A DFT study of the electronic, optical and topological properties of free and biaxially strained CuIn 1–x Al x Se 2

Pingping Jiang, P. Boulet, Marie-Christine Record

A DFT study of the electronic, optical and topological properties of free and biaxially strained $CuIn_{1-x}Al_xSe_2$

Pingping JIANG [a,b], Pascal BOULET [a], Marie-Christine RECORD [*b]

[a] Aix-Marseille University, CNRS, MADIREL, Marseille, France

[b] Aix-Marseille University, University of Toulon, CNRS, IM2NP, Marseille, France

Abstract

The electronic and optical properties of free and biaxially strained $CuIn_{1-x}Al_xSe_2$ have been calculated by using the full potential linear augmented plane wave (FP-LAPW) method. Results show that $CuIn_{1-x}Al_xSe_2$ has a direct band gap with increasing value as x increases. $CuIn_{0.75}Al_{0.25}Se_2$ has been recognized as the optimal substituted compound in terms of band gap and conversion efficiency. Geometry optimized bond length and bond angle between nuclei terminal atoms (M, Se) and bond critical point, electron density ρ, local energy density, and Laplacian $\nabla^2\rho$ for nonequivalent pairwise M-Se have been examined. High bond deflection with small bond angle gives high possibility of electron transition, which mainly occurs between In and Se orbitals. Under biaxial strains, the optical properties are improved along the lengthened deformation direction.

Keywords: DFT; $CuIn_{1-x}Al_xSe_2$; Optical properties; Electron density topological properties; Biaxial strain.

1. Introduction

The conversion of solar energy into electricity, namely photovoltaic (PV) effect, has been regarded as a competitive and attractive substitute to other energy conversion forms due to its tremendous advantages[1,2]. However, the photovoltaic conversion efficiency of semiconductors (SCs) needs materials with appropriate band gap (Eg). Hence, due to the materials incapability to absorb photons of energy lower than Eg and to the low conversion efficiency, caused by thermal losses, when photon energy is far higher than Eg, we have to explore more adaptable PV materials[3,4]. The ternary Cu-based chalcopyrite compound, $CuInSe_2$ (CIS), is an interesting material as solar cell absorber layer due to its low cost, high absorption coefficient, excellent optical and electrical properties. Many approaches have been adopted to improve the energy conversion efficiency[5]. However, its narrow band gap and the scarcity and expensiveness of indium constrain its large-scale development. Substituting indium with the abundant and inexpensive aluminum to form the quaternary SC, $CuIn_{1-x}Al_xSe_2$ (CIAS), has been considered as a promising alternative with few changes in physical and chemical properties[6].

A general trend is that the band gap decreases in moving down in a periodic table group[7]. Theoretically, the optical band gap of CIAS can be varied from 1.04 eV to 2.67 eV as aluminum ratio x goes from 0 to 1[8]. Compared to Ga-doped $CuInSe_2$, CIAS allows for reaching higher energy band gap with less aluminum content, therefore fewer lattice distortion and defects. Several experimental researches have been conducted on CIAS, attempting to find the optimal substitute content based on the structural, optical and electronic properties[8–11]. Aluminum substitution not only increases the band gap, as found by López-García et al[11] on the way to study CIAS (x=0~0.6) thin film, but also changes the carrier density and mobility. As found by

Cheng et al[10], due to low formation energy the main acceptors Cu vacancies decreased as x increased, contributing to such carrier mobility that materials yield the highest photovoltaic performance when x is 0.34. Besides, density functional theory (DFT) has been applied in solar cells area for many years to calculate the structural, electronic and optical properties[12,13]. The agreement between the calculated data and the experimental ones proved the validity of regarding numerical calculations as an adequate method for PV materials studies[14–16]. By calculating the optical properties, Tang et al[17] found that $CuIn_{0.75}Al_{0.25}Se_2$ is a suitable PV material in considering both band gap and optical properties.

The quantum theory of atoms in molecule (QTAIM) proposed by Bader et al[18] has evolved to be an invaluable tool for the chemical interpretation of quantum mechanical data. This theory is built upon quantum mechanical observable quantities, such as the electron density ρ. By inspecting the electron density within the quantum theory framework and analyzing the interatomic interactions through the topological analysis of ρ, a comprehensive characterization from the strong shared-shell (SS) to weak closed-shell (CS) interactions has been concluded. The classification of the SS- and CS-type of interactions is based on the negative and positive sign of the Laplacian of ρ at their bond critical points (BCPs), respectively. However, it was found that such a simple classification in description of these bonds is not meticulous enough, particularly in complex situation[19]. A more specific quantitative scale is then needed. The local energy density obtained by integrating along each basin, the electron density flatness, the charge transfer, and the bond degree have been proposed to better characterize the interatomic interactions[19–21]. Saeed et al[22] found that for Ag-based chalcopyrite materials, $AgXY_2$ (X=Al,Ga,In and Y=S,Se,Te), the positive Laplacian of pairwise Ag-Y at BCP characterizes an ionic bond, while the negative Laplacian of the pairwise X-Y at BCP reveals a covalent character. For Cu-based chalcopyrite materials, a comprehensive study of all the topological and energetic properties in the full range of interactions has never been undertaken. Analysis of these properties based on the electron density could help us to clarify the optical behaviors systematically. This can be obtained from the evolution of chemical pairwise interactions as aluminum substitutes indium, giving a chance to shed light on the inner relationship between the topological and optical properties.

In current PV cells, strains originating during their fabrication from the lattice mismatch between the PV materials and the substrates inevitably influence the optical performances. Researches have been conducted on the structure, electronic and optical properties under uniaxial and biaxial strains[23–25]. Some researchers even studied the phase stability, electronic properties and chemical bonds of $CuIn(Al,Ga)Se_2$ under high isotropic pressure by DFT[26]. It was found that materials underwent a phase transition that could even lead to non-semiconductor materials, as with $CuGaSe_2$ for which covalent bonds are strengthened. Studying the influence of strains on photovoltaic materials properties is hence indispensable.

In this work, by DFT calculations we studied the structural, electronic and optical properties of $CuIn_{1-x}Al_xSe_2$ (x=0, 0.25, 0.5, 0.75 and 1), and determined the optimal substituting percentage. At this optimal value, we calculated the band gap and optical properties for the material subjected to biaxial strains. Besides, in the aim to unravel the deep relationship between bond interactions and optical properties, a detailed investigation of topological properties based on the electron density has been conducted as strain is applied.

2. Computational details

We performed first principle density functional theory calculations using the full potential linear augmented plane wave (FP-LAPW) method based on Kohn-Sham equations, as implemented in WIEN2k package[27]. The generalized gradient approximation (GGA) approach has been used to describe the exchange-correlation energy[28]. $CuInSe_2$ has tetragonal structure (space group I-42d), each selenium ion being coordinated with 2 indium and 2 copper ions, and each indium and copper ion being coordinated with four selenium ions, as shown in the inset of **Fig. 1**. The core-valence electrons separation has been defined as follows: Cu $[Ar]3d^{10}4s^1$, In $[Kr]4d^{10}5s^25p^1$, Al $[Ne]3s^23p^1$, Se $[Ar]3d^{10}4s^24p^4$. The Muffin-tin radii for Cu, In, Al and Se atoms were 2.35, 2.42, 2.24 and 2.24 a.u. respectively. First, we performed structure optimization with PBE-, PBEsol- and WC-GGA. We obtained the optimized lattice parameters by calculating the total energy with respect to the crystal cell volume and c/a ratio in sequence. The fitting result, as shown in **Fig. 1**, was obtained by using the Birch-Murnaghan equation of state:

$$E(V) = E_0 + \left({}^{9V_0}/_{16}\right)\left({}^{B}/_{14703.6}\right)(\eta^2-1)^3 B_P + (\eta^2-1)^2(6-4\eta^2) \quad (1)$$

$$\eta = \left({}^{V_0}/_{V}\right)^{\frac{1}{3}} \quad (2)$$

where V_o, V present the initial and deformed volume respectively, B is the bulk modulus, B_P is the derivative of bulk modulus with respect to pressure.

After the lattice constants have been optimized, a full relaxation was operated on the whole structure until the total residual forces on all atoms were less than 2 mRy/bohr. **Table 1** displays the optimized lattice parameters and bond lengths in comparison to the experimental values of $CuInSe_2$ and $CuAlSe_2$. We can see that, the calculated lattice parameters match the experimental values within a reasonable range of errors and WC-GGA provides the best agreement with respect to experiments. The plane wave cutoff parameter $R_{MT}K_{max}$ in the interstitial region was set to 7, where R_{MT} is the smallest atomic sphere radii and K_{max} is the maximum value of the reciprocal lattice vector in the plane wave expansion. In the interstitial region the charge density and potential were expanded as a Fourier series with wave vectors up to G_{max}=14 $a.u^{-1}$. The Brillouin zone were sampled with a mesh of 1500 k-points using Monkhorst-Pack grids[29]. These calculating conditions were also adopted in the indium substituted cases. **Fig. 2** presents the lattice parameters and their fitting results as Al content x varies. As x increases, lattice a and c decrease linearly, respectively. Bodnar et al[30] studied the $CuAlSe_2$-$CuInSe_2$ phase diagram, confirms that there is a complete solid solution from $CuAlSe_2$ to $CuInSe_2$. **Table 2** lists the formation energy of $CuIn_{1-x}Al_xSe_2$ when x is 0.25, 0.5 and 0.75 respectively. In-substituted systems are stable due to their negative formation energy.

The biaxial strains have been simulated according to the deformation ratios of ±4%, ±3%, ±2%, ±1%, and 0% with respect to the equilibrium in-plane lattice a perpendicular to c-axis in conditions of constant volume. Negative and positive signs stand for the compressive and tensile in-plane strain, respectively. For each applied constrain the relaxed value of c and u(Se) were calculated. Then, band structure, dielectric constant and absorption coefficient have been calculated as well. As for the topological properties, program CRITIC2[31] has been used for the real space analysis of quantum chemical interactions. In QTAIM, the partitioning in atomic

regions, called basin, is determined uniquely by the zero-flux surfaces of the electron density ρ. The kinetic, potential and total energy density, volume and charge can be obtained by the integration in the basins with the electron density calculated by WIEN2k.

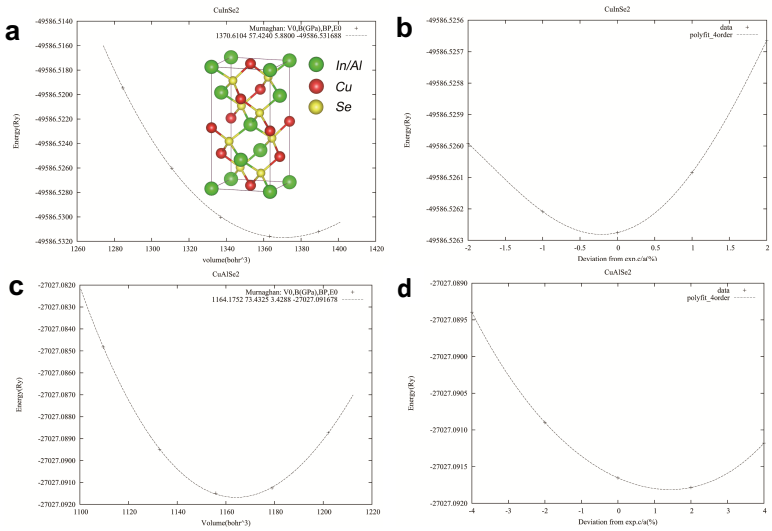

Fig. 1 Structure optimization of $CuInSe_2$ (a) (b) and $CuAlSe_2$ (c) (d).

Table 1

Lattice parameters a and c and bond lengths d(Å) of $CuInSe_2$ and $CuAlSe_2$. u(Se) is the free x-coordinate of Se in the chalcopyrite unit cell.

		GGA functionals	a	c	u(Se)	c/a	$d_{Cu\text{-}Se}$	$d_{In\text{-}Se}$	$d_{Al\text{-}Se}$
$CuInSe_2$	Exp.[32]		5.7815	11.6221	0.2426	2.0102	2.5326	2.4833	-
	Calc.	PBE	5.8798	11.7672	0.2688	2.0013	2.5723	2.5236	-
		PBEsol	6.0369	11.9387	0.2814	1.9776	2.4430	2.6551	-
		WC	5.8775	11.7565	0.2683	2.0002	2.4845	2.6089	-
$CuAlSe_2$	Exp.[33]		5.6060	10.9010	0.2600	1.9443	2.4383	-	2.3729
	Calc.	PBE	5.5307	10.7536	0.2506	1.9443	2.3748	-	2.3709
		PBEsol	5.5983	11.0090	0.2571	1.9443	2.3878	-	2.4340
		WC	5.6194	10.9261	0.2506	1.9443	2.4129	-	2.4089

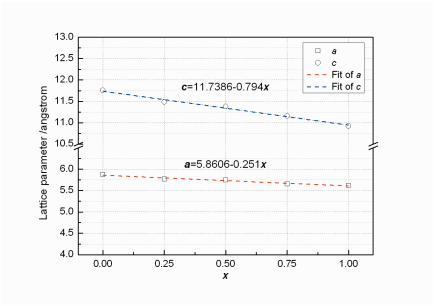

Fig. 2 Lattice parameters and their fitting results as aluminum content x varies.

Table 2

Formation energy ∇f of In-substituted system when x equals to 0.25, 0.5 and 0.75, respectively.

x	0.25	0.5	0.75
∇f/eV	-0.681	-1.50	-2.46

3.Results and discussion

3.1 Investigation of the $CuIn_{1-x}Al_xSe_2$ alloys

3.1.1 Band structure

The band structures of $CuIn_{1-x}Al_xSe_2$ alloys (x=0, 0.25, 0.5, 0.75, and 1) are plotted in **Fig. 3** along the high symmetry directions in ***k***-space. The dashed horizontal line in band structure shows the position of Fermi level energy (E_F), and was set to zero as reference in this work. The values of band gap Eg can be obtained from the energy difference between conduction band minimum (CBM) and valence band maximum (VBM). The highest valence band states originate from a threefold-degenerate p orbital. Both the CBM and the VBM occur at Γ point, the center of the first Brillouin zone, indicating a direct band gap. As shown in **Fig. 3f**, the band gap increases continually as x increases. This trend is in accordance with the experiment results[9,17], though the values have been underestimated by GGA functional because of the inaccurate calculation of exchange-correlation energy[34,35].

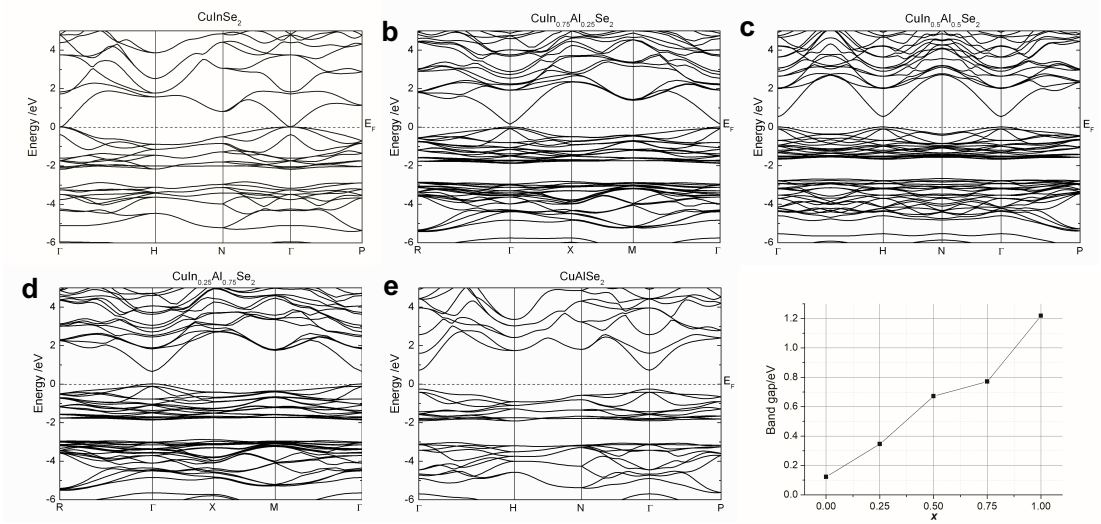

Fig. 3 Band structures of $CuIn_{1-x}Al_xSe_2$ when x equals to 0 (a), 0.25 (b), 0.5 (c), 0.75 (d), 1 (e), and their corresponding band gap (f).

3.1.2 Density of states

We use the equilibrium geometries obtained from full relaxation of the $CuIn_{1-x}Al_xSe_2$ systems to calculate their total and partial density of states (TDOS and PDOS), which are shown in **Fig. 4**. The TDOS can be divided into four regions (**Fig. 4a**). Since the inter-band transition occurs mostly at the vicinity of the Fermi level and no intra-band contributions were added in our study, our main consideration on PDOS focuses in the [-6;10] eV energy region, as shown in **Fig. 4b-f**. The PDOS presents the contributions to TDOS of different orbitals states for each atom in the system. Fully occupied d orbitals of indium and selenium atoms have not been considered in our investigation. One can see that the valence band is dominated by copper 3d and selenium 4p with the strongest mixing between these orbitals in the upper side of valence band ranging from -2 eV up to the Fermi level. This is consistent with the results in Ref.[14,15]. From -4 eV to-3.2 eV, in addition to Cu d and Se p orbitals, there is a small contribution of In p and Al p orbitals in the mixing. In the region of [-5.4;-4.6] eV, we observe a comparatively strong hybridization of Cu s and Se p states. Conduction band between 1.5 eV and 2.5 eV is

characterized by a mixing of In 5s and In 5p, when present in the system, Cu 3d and Se 4p orbitals. Moreover, the densities of these orbitals are at a higher level when x=0.25 than others. In the aluminum containing compounds, Al 3s and Al 3p orbitals also contribute to the PDOS.

The ionic and covalent character of a bond can be determined by the difference of electronegativities between two bonded atoms[36]. Large differences provide an ionic bond due to charge transfers between atoms. By contrast, small differences feature covalent bond due to charge sharing. According to Duffy[37] there is a relationship between band gap and electronegativity, as expressed by $\upsilon_{max} = 30000\left[\chi_{opt}(\text{anion}) - \chi_{opt}(\text{metal ion})\right]$, where υ_{max} is the onset of optical absorption, χ_{opt} is the optical electronegativity. The decrease of band gap is accompanied by a decrease of ionicity in bonding, which arises from a decreased electronegativity difference. Verma[38] found a linear relationship between band gap and optical electronegativity of solids; $CuInSe_2$ has lower optical electronegativity, 0.588, than $CuAlSe_2$, 0.736, which corresponds to its smaller band gap than the latter one. As the aluminum content x increases, the band gap keeps increasing since the optical electronegativity is enlarged continuously. Thus, for a given incident photon wavelength fewer electrons can jump from valence band to conduction one.

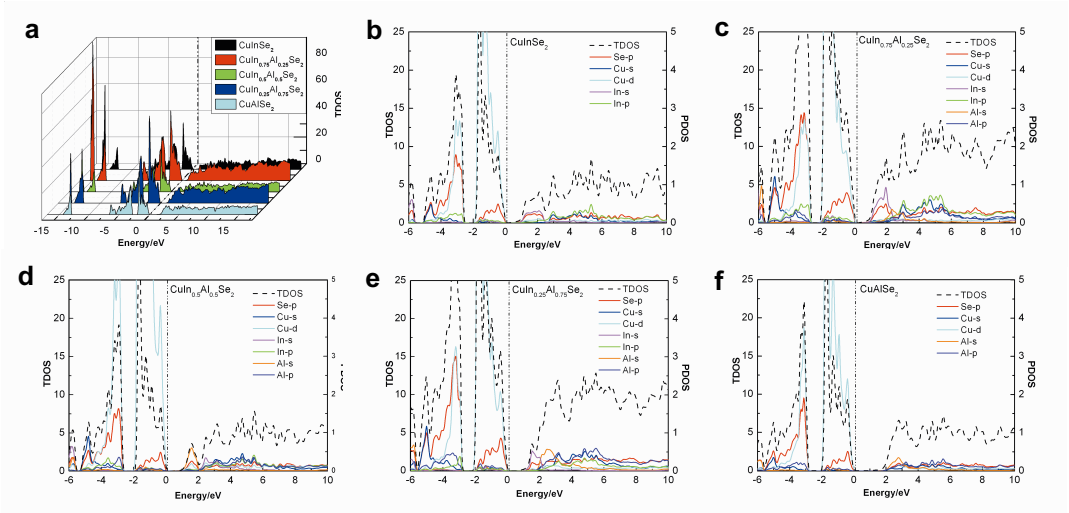

Fig. 4 Total density of states (a) and partial density of states of $CuIn_{1-x}Al_xSe_2$when x equals to 0 (b), 0.25 (c), 0.5 (d), 0.75 (e), and 1 (f).

3.1.3 Optical properties

The optical properties of materials, which correspond to the response of materials to an electromagnetic perturbation, can be accessed by the calculation of the frequency-dependent complex dielectric functions $\varepsilon(\omega) = \varepsilon_1(\omega) + i\varepsilon_2(\omega)$. The imaginary part $\varepsilon_2(\omega)$ is calculated using the following formula:

$$\varepsilon_2(\omega)=\frac{e^2\hbar}{\pi m^2\omega^2}\sum_{v,c}\int_{BZ}|M_{cv}(k)|^2\delta\{\omega_{cv}(k)\omega\}\,d^3k \quad (3)$$

where $M_{cv}(k)$ are the momentum matrix elements between occupied (valence) and unoccupied (conduction) states, the sums are performed on all the valence and conduction states and the k-points of the first Brillouin zone. The real part $\varepsilon_1(\omega)$ is calculated using Kramers-Kronig relation:

$$\varepsilon_1(\omega) = 1 + \frac{2}{\pi}P\int_0^{\infty}\frac{\omega'\varepsilon_2(\omega')}{\omega'^2 - \omega^2 + i\eta}d\,\omega' \quad (4)$$

where P is the principal value of the integral and η is an infinitesimal number.

As $\varepsilon_1(\omega)$ and $\varepsilon_2(\omega)$ strongly depend on the band structure, it must then be properly described. For this, a scissor operator has been used to correct for the underestimated gap with respect to the experimental value. Both the real and imaginary parts of $\varepsilon(\omega)$ are plotted along the perpendicular (*xx*) and parallel (*zz*) directions to the *c*-axis for $CuInSe_2$ and $CuAlSe_2$ in **Fig. 5**. The calculated results are compared to experimental ones obtained in Ref.[39,40] from spectroscopic ellipsometry. As it shows, our calculation fits the experimental trends quite nicely, better than Ref. [17] (not shown here), supporting again that our calculation settings lead to an accurate description of the optical properties.

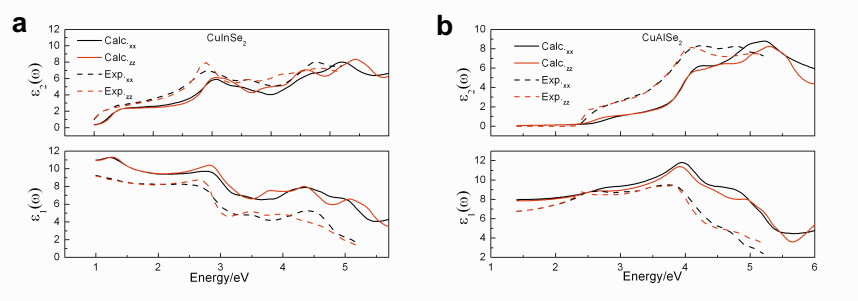

Fig. 5 Calculated (solid lines) and experimental (dash lines) results of dielectric functions of $CuInSe_2$ (a) and $CuAlSe_2$ (b) in the perpendicular (*xx*, black lines) and parallel (*zz*, red lines) directions to *c*-axis. The experimental data are taken from Ref.[39,40].

Fig. 6 shows the dielectric functions $\varepsilon_1(\omega)$ and $\varepsilon_2(\omega)$, and absorption coefficient $\alpha(\omega)$ for $CuIn_{1-x}Al_xSe_2$. Rybicki and Lightman[41] state that the absorption coefficient indicates the travelling displacement a photon could have before being absorbed by the materials. It can be obtained directly from the dielectric function. As the experimental gaps of the $CuIn_{1-x}Al_xSe_2$ when x is in between 0 and 1 are unknown, the scissor operation was not applied for these compounds in considering the consistency.

The evolutions of optical responses at perpendicular and parallel directions conform to each other. The decreasing imaginary part $\varepsilon_2(\omega)$ as well as the right shift of the peaks as *x* increases from 0 to 1 when the incident energy is lower than 2.5 eV can be interpreted as the decreasing ability to absorb some light wavelengths. This can be correlated to the enlarged band gap as *x* increases. Incident photons with high enough energy can be absorbed by large band gap material to trigger the electrons transition, while they are mainly wasted in small band gap materials through heat relaxation.

The static dielectric function $\varepsilon_1(0)$ and frequency-dependent $\varepsilon_1(\omega)$ are related to the band gap energy since they are obtained from the imaginary part $\varepsilon_2(\omega)$. The Penn model[42] exhibits an inverse relation between $\varepsilon_1(0)$ and the square of the band gap energy *Eg*, $\varepsilon_1(0) \cong 1 + (\hbar\omega/Eg)^2$, where $\hbar\omega$ is the plasma energy. From **Fig. 6a**, $\varepsilon_1(0)$ decreases from 17 to 8.5 as *x* increases from 0 to 1, which reflects an increase in optical band gap since higher $\varepsilon_1(0)$ gives lower band gap. The fluctuation of $\varepsilon_1(\omega)$ in the energy range from *Eg* to around 6 eV indicates the interaction of material with the photons.

Regarding the absorption coefficient (**Fig. 6b**) one can note that the calculated absorption edge values are consistent with variation of band gaps at the center of the first Brillouin zone. With increasing incident photon energy, the absorption coefficient increases to reach a maximum value around 9 eV with various small peaks in between, corresponding to electron transitions from the valence band to the conduction one. In the energy range of [0;6] eV, which

corresponds to the most intense part of sun radiation, the absorption coefficient decreases as *x* increases. The absorption peaks experience a right shift in the range [0;4] eV and a left shift in the range [4;6] eV. Above 6 eV, the absorption coefficients of all the compounds increases sharply to their maximum; $CuAlSe_2$ absorption coefficient is the highest. Spectroscopic limited maximum efficiency (SLME) has been recognized as a useful method to characterize the PV abilities of materials[43]. For a real solar cell, the theoretical maximum efficiency depends on the thickness of the absorber layer[44]. In the energetic domain [1.5;3.1] eV, the maximum efficiency η of $CuIn_{1-x}Al_xSe_2$ has been calculated with respect to the absorber thickness, as shown in **Fig. 6c**. The substituted system displays a decreasing η as *x* goes from 0 to 1 at any given thickness. The maximum one corresponds to pure $CuInSe_2$, whereas among all the $CuIn_{1-x}Al_xSe_2$ alloys, that with x equals 0.25 has the highest conversion efficiency. Accordingly, $CuIn_{0.75}Al_{0.25}Se_2$ is a promising PV material for the fabrication of solar cells in considering the good trade-off between a large enough band gap and a relatively high conversion efficiency.

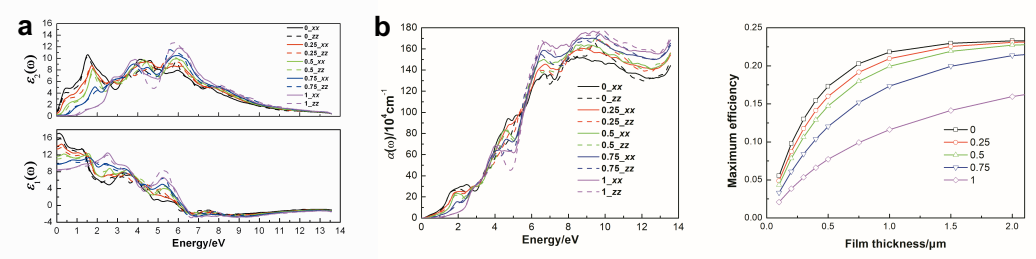

Fig. 6 Dielectric functions (a) and absorption coefficient (b) for $CuIn_{1-x}Al_xSe_2$ at different *x* values. The solid lines and dashed lines represent the perpendicular (*xx*) and parallel (*zz*) directions to *c*-axis, respectively. Calculated maximum efficiency (c) with respect to the film thickness in the energetic domain [1.5;3.1] eV.

3.1.4 Topological properties

To unravel the possible relationship between optical properties and topological properties of the electron density, the influence of aluminum substitution has also been investigated on topological properties. **Fig. 7** shows the electron density and Laplacian distributions for the optimal indium substituted compound, $CuIn_{0.75}Al_{0.25}Se_2$, in both planes (110) and (-110). Electron density diagrams serve as a complementary tool to achieve a proper understanding of the electronic structure. Bader's theory defines critical points that are saddle points in the charge density on the zero-flux surfaces. Bond critical points are critical points on bond paths, the paths between bonded atoms along which the charge density is at a maximum with respect to that along any neighboring paths. It is found that there is a correlation between the values of the electron density at the bond critical points (BCPs) and the interaction strength between atoms[45]. The properties at the BCPs between Cu, In, Al nuclei and Se ones (M-Se) constitute our main subject of interest.

Besides, the Laplacian of the electron density ($\nabla^2\rho_{BCP}$) at BCPs provides details analogous to those found in relation to ρ_{BCP}. According to the local virial theorem, the Laplacian can be expressed in function of the kinetic G_{BCP} and potential V_{BCP} energy density as $\hbar^2/4m\,\nabla^2\rho_{BCP} = 2G_{BCP} + V_{BCP}$[46,47]. The ionic character of a material can be related to charge transfer between cations and anions while covalent character is related to charge sharing. In the present case, there are Cu-Se, Al-Se and In-Se interactions leading to the building of crystal orbitals. It is hence essential to find out their featuring attributes. **Table 3** lists the bond distances

defined along the "n-b-n" path (where "n" are the nuclei and "b" is the bond critical point), the electron density ρ_{BCP}, the Laplacian $\nabla^2\rho_{BCP}$, local electron kinetic G_{BCP}, potential V_{BCP} and total H_{BCP} energy densities, as well as the parameters related to the bonding characters at the non-equivalent bond critical points in unit cell. The results presented below concern the two tetrahedron sub-structures, structure I and structure II (inset of **Fig.9**), which build up all the compounds. Structure I is composed of four types of atoms, namely Cu, In, Al and Se, while structure II is composed of three types of atoms, namely Cu, In, Se or Cu, Al, Se. For *x* equals to 0 and 1 only structure II is present whereas for x equals 0.5 only structure I is present. Structure I and structure II both exist when *x* is 0.25 and 0.75. we use the asterisk sign (*) to represent the longest bond length for each pairwise M-Se.

Fig. 8 depicts the bond lengths and bond angles for each pairwise M-Se, both being determined from "n-b-n" path, where "n" are the nuclei and "b" is the bond critical point. As it shows, for a given value of *x* the bond lengths and angles behave oppositely. For example, M-Se* has a longer bond length and a lower angle than M-Se. In-Se has the smallest angle which accords with its longest bond length in comparison to Cu-Se and Al-Se. This dependence on bond length and angle provides a gauge to evaluate the bond interaction in Cu-chalcogenide materials.

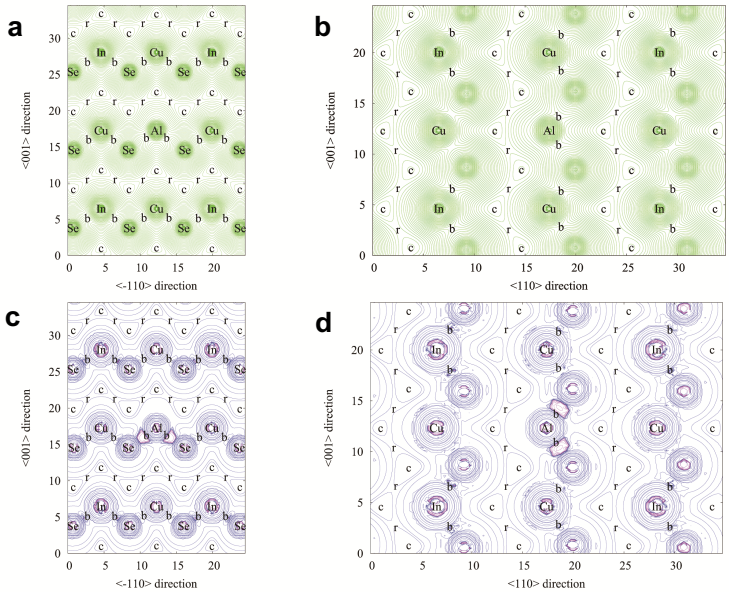

Fig. 7 Electron density (top panels) and Laplacian (bottom panels) distribution of $CuIn_{0.75}Al_{0.25}Se_2$ in plane (110) (a) (c) and plane (-110) (b) (d). b, c, and r mean bond, cage, and ring critical points. Green lines represent the electron density ρ, magenta and blue lines represent the negative and positive $\nabla^2\rho$, respectively.

Table 3

Topological and energetic properties of each pairwise M-Se. Associated units: bond length (Å) defined along the "n-b-n" path (where "n" are the nuclei and "b" is the bond critical point), ρ_{BCP} (10^{-2}e·Å^{-3}), $\boldsymbol{\nabla^2\rho_{BCP}}$ (10^{-2}e·Å^{-5}), G_{BCP}, V_{BCP}, H_{BCP} (10^{-2}kJ/mol per atomic unit volume), and H_{BCP}/ρ_{BCP} (kJ/mol per electron). I and II correspond to two different tetrahedron structures (see text), as depicted in the inset of **Fig.9**. The asterisk sign (*) means the longest bond length for each pairwise M-Se.

x	M-Se	Bond length	ρ_{BCP}	$\nabla^2\rho_{BCP}$	G_{BCP}	V_{BCP}	H_{BCP}	$\lvert V_{BCP}\rvert/G_{BCP}$	H_{BCP}/ρ_{BCP}
0	Cu-Se^{II}	2.4363	6.023	10.414	4.393	-6.182	-1.789	1.407	-0.297

	In-Se^{II}	2.6644	5.446	7.017	3.416	-5.078	-1.662	1.487	-0.305
0.25	Cu-Se^{I}	2.4215	6.175	11.223	4.64	-6.474	-1.834	1.395	-0.297
	-Se*^{I}	2.4300	6.072	11.144	4.551	-6.316	-1.765	1.388	-0.291
	Cu-Se^{II}	2.3925	6.070	11.823	5.006	-7.057	-2.050	1.410	-0.314
	-Se*^{II}	2.4016	6.408	11.623	4.884	-6.862	-1.978	1.405	-0.309
	In-Se^{I}	2.6337	5.715	7.470	3.679	-5.491	-1.812	1.492	-0.317
	-Se^{II}	2.6247	5.818	7.608	3.776	-5.650	-1.874	1.502	-0.322
	-Se*^{II}	2.6365	5.711	7.394	3.664	-5.480	-1.816	1.496	-0.318
	Al-Se^{I}	2.4487	5.311	6.514	3.240	-4.852	-1.612	1.497	-0.304
0.5	Cu-Se^{I}	2.4339	6.035	10.864	4.477	-6.238-6.069	-1.761-1.693	1.393	-0.292
	-Se*^{I}	2.4427	5.927	10.732	4.376			1.387	-0.286
	In-Se^{I}	2.6321	5.730	7.298	3.662	-5.499	-1.837	1.496	-0.321
	Al-Se^{I}	2.4308	5.436	7.248	3.448	-5.083	-1.636	1.474	-0.301
0.75	Cu-Se^{I}	2.3962	6.460	11.815	4.955	-6.957-6.885	-2.002-1.972	1.401	-0.310
	-Se*^{I}	2.4003	6.416	11.763	4.913			1.404	-0.307
	Cu-Se^{II}	2.4076	6.321	11.544	4.804	-6.722-6.330	-1.918-1.772	1.396	-0.293
	-Se*^{II}	2.4274	6.086	11.183	4.567			1.388	-0.291
	In-Se^{I}	2.6084	5.966	7.736	3.905	-6.339	-1.971	1.505	-0.330
	Al-Se^{I}	2.4257	5.488	7.450	3.517	-5.172	-1.655	1.471	-0.302
	-Se^{II}	2.4210	5.508	7.645	3.564	-5.216	-1.652	1.464	-0.300
	-Se*^{II}	2.4372	5.392	6.986	3.374	-5.002	-1.628	1.482	-0.302
1	Cu-Se^{II}	2.4129	6.251	11.364	4.721	-6.600	-1.880	1.398	-0.301
	Al-Se^{II}	2.4089	5.602	8.115	3.707	-5.385	-1.678	1.453	-0.300

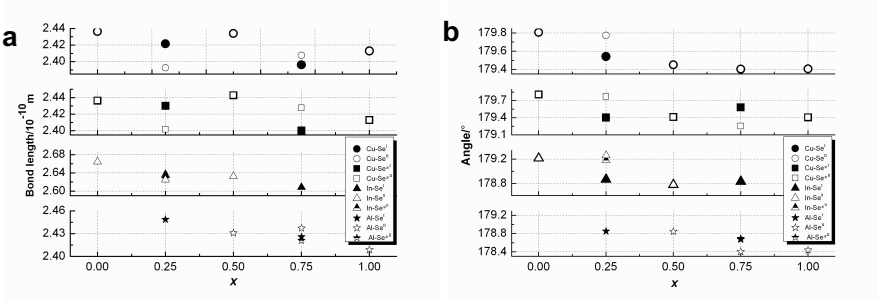

Fig. 8 Calculated bond lengths (a) and bond angles (b) in $CuIn_{0.75}Al_{0.25}Se_2$. I and II correspond to two different tetrahedron structures (see text), as depicted in the inset of **Fig. 9**. The asterisk sign (*) stands for the longest bond length for each pairwise M-Se. Both the bond lengths and angles are determined along the "n-b-n" path, where "n" are the nuclei and "b" is the bond critical point, respectively.

The sign of $\nabla^2\rho_{BCP}$ is a useful tool to distinguish the types of interactions between atoms. From a topological point of view, pure closed-shell (CS) charge-depletion interactions at BCP are marked with a low electron density and a positive Laplacian in ionic crystals (e.g. ionic bond, hydrogen bond and van der Waals interactions).The BCPs are characterized by the relatively large value of the kinetic energy density and a positive value of the total energy density[48]. By contrast, pure shared-shell (SS) exhibits a negative Laplacian with locally

concentrated electron density (e.g. covalent and polar bonds), dominated by the potential energy density, the total energy being negative. These two types of definition are not enough though to describe the bonding properties since most crystals do not belong to these extreme prototypes. Espinosa et al.[21] divided the bond types into three classes by using the adimensional $|V_{BCP}|/G_{BCP}$ ratio and introducing the bond degree (BD=H_{BCP}/ρ_{BCP}). In addition to the pure CS ($|V_{BCP}|/G_{BCP}<1$) and SS ($|V_{BCP}|/G_{BCP}>2$), another region named *transit* CS with positive Laplacian and negative total energy density ($1<|V_{BCP}|/G_{BCP}<2$) has been defined, as plotted in **Fig. 9**, that shows the BD versus $|V_{BCP}|/G_{BCP}$. The interactions of Cu-Se, In-Se, and Al-Se all lie in the *transit* CS zone, between the typical ionic and covalent bonds. Our results are in agreement with Saeed et al.[22] ones that render the covalent character with a weak polarization between Al, Ga, In cations with S, Se and Te anions.

Since for the tetrahedron structures I and II, electrostatic interactions between metal and Se ions are nonequivalent due to the aluminum substitution, the corresponding bonds have been divided into M-Se and M-Se* according to their bond lengths, as described above. In structure I, as x increases, the absolute magnitudes of the bond degree, i.e. covalence degree (CD) when $H_{BCP}<0$[21], of Cu-Se and Cu-Se* first decrease (from x=0 to x=0.5), then increase to a maximum (at x=0.75) and finally decrease as x goes to 1. While in structure II, the CD of Cu-Se and Cu-Se* first increase to a maximum (at x=0.25), then decrease sharply to a minimum (at x=0.5) and goes up again to x=1. The CD maxima for Cu-Se/Se* in structure I and II occur at 0.75 and 0.25, respectively, as well as in In-Se case. As x increases, the CD of In-Se increases while that of Al-Se decreases, and In-Se has stronger bond interaction compare with that of Cu-Se/Se* and Al-Se/Se* for each x value due to its higher covalent degree. This is consistent with Wada's results[49].

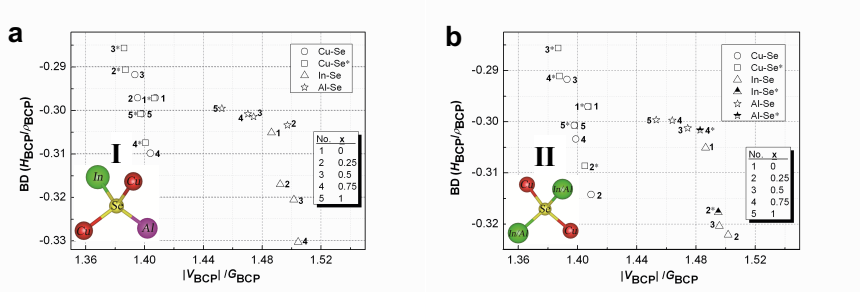

Fig. 9 Values of bond degree (BD=H_{BCP}/ρ_{BCP}) vs. $|V_{BCP}|/G_{BCP}$ at BCPs of M-Se as x varies from 0 to 1. Structures I (Cu/In/Al-Se, a) and II (Cu/In-Se or Cu/Al-Se, b) represent two different constitutive parts of every unit cell. The asterisk sign (*) stands for the longest bond length for each pairwise M-Se.

In addition, it is noticeable that the evolution between covalent degree (i.e. bond degree) and $|V_{BCP}|/G_{BCP}$ ratio agrees with each other, i.e. the higher the degree, the bigger the ratio. Negative total energy density is the sign of nuclei attraction. When two atoms share electrons to form a covalent bond, bond degree can be interpreted as the intensity of bond attraction. The $|V_{BCP}|/G_{BCP}$ left shift of Al-Se and $|V_{BCP}|/G_{BCP}$ right shift of In-Se as x increases reflect to a stronger nuclei attraction of In-Se than Al-Se. As listed in **Table 3,** the accumulation of electron density at BCP along each bond path increases almost linearly as the bond length decreases. Small bond length means large overlapping space in electron cloud. Generally, any mechanism that increases electron density in material also increases refractive index. The ease of electron transition from Se^{2-} anion full valence band to empty metal conduction band determines the

optical response in the presence of incident photons. In-Se, with its largest bond degree compared to that of Cu-Se/Se* and Al-Se, contributes the most to the high absorption coefficient of $CuInSe_2$ since the Se 4p and In 5s+5p orbitals are prominent in the valence and conduction states, respectively, near the Fermi level. These orbitals contributions may also explain the much lower band gap of $CuInSe_2$ than that of $CuAlSe_2$. In effect with increasing aluminum content in $CuIn_{1-x}Al_xSe_2$, the In 5s+5p orbitals contribute less and less to the conduction band, while the contribution of Al 3s+3p is gradually increasing. Moreover, since the Al orbitals contribution to the DOS increases, the decreasing covalent bond degree of Al-Se prevails over the In-Se increasing one, which leads to an overall decrease of the covalent bond degree. Interestingly, a correlation can be made between the maximum covalent bond degrees in **Fig. 9** and the partial density of states in conduction band in **Fig. 4**, that gives a basis to evaluate the optical response. In **Fig. 4c** (x=0.25), the peaks at 1.6 eV and 3.2 eV of the conduction band, which are mainly contributed from Se 4p and In 5s orbitals, and In 5p and Cu 4s ones respectively, can be correlated to the covalent bond degree maxima of Cu-Se/Se* and In-Se in structure II (see **Fig. 9**), originating from the transitions of electrons between Se 4p and In 5s+5p/Cu 4s hybrid orbitals. Likewise, the maxima of Cu-Se/Se* and In-Se in structure I can be correlated to the peaks in **Fig. 4e** (x=0.75). These results show that, pairwise In-Se contributes the most to electron transition compare to other pairwises for the In-substituted compound.

3.2 Investigation of $CuIn_{0.75}Al_{0.25}Se_2$ under strains

From the above results, $CuIn_{0.75}Al_{0.25}Se_2$ compound has been chosen as target to perform the biaxial strain study. The evolution of atomic geometry parameters under compressive (-) and tensile (+) in-plane strain is shown in **Fig.10**. As expected, due to the constant volume lattice relaxation, there is a linear decrease of c/c_0 and c/a in the strain range [-4%;+4%]. In the meantime, u(Se), which is the free x-coordinate of Se in the structure decreases linearly as can be seen from the fitting curve in **Fig. 10c**.

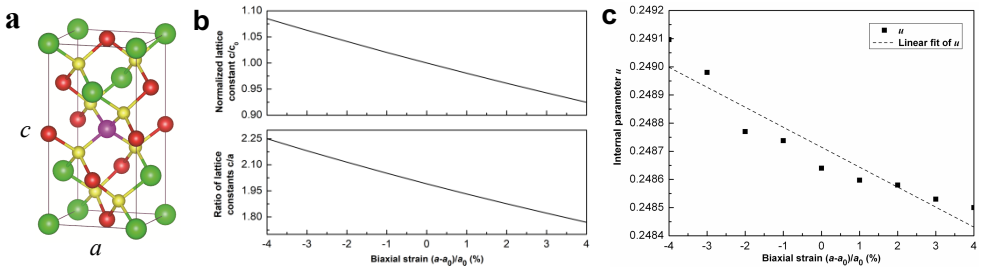

Fig. 10 Geometric characteristics of $CuIn_{0.75}Al_{0.25}Se_2$ and their evolution under biaxial strains $(a-a_0)/a_0$. Unit cell (a), green, red, yellow and magenta atoms represent In, Cu, Se and Al, respectively. lattice constant ratio c/c_0 and c/a (b) and internal parameters u(Se) (c).

3.2.1 Optical properties

Band gap, absorption coefficient and dielectric functions along perpendicular (xx) and parallel (zz) directions to c-axis of $CuIn_{0.75}Al_{0.25}Se_2$ under strain are shown in **Fig. 11** and **Fig. 12**. Band gap decreases for both compressive and tensile strains, and it decreases faster under compressive strains than under tensile ones. In-plane (α_{xx}) and out-of-plane (α_{zz}) absorption coefficients behave oppositely under strains. No evident dispersion of $\alpha(\omega)$ occurs when incident energy is below 1.6 eV, except a slight decrease for α_{xx} and a slight increase for α_{zz} as

strain goes from compressive to tensile. For incident energy above 1.6 eV, strains favour the dispersions with significant rise of α_{xx} and fall of α_{zz} from compression to tension. As it shows, positive strain, which lengthens the lattice *a* and shortens the *c* one, provides a bigger chance to absorb incident photons along the *xx* direction than along the *zz* one. Conversely, the negative strain will result in a bigger chance to absorb incident photons in the *zz* direction than in the *xx* one. This is consistent with the essay to extend the optical path for increasing the effective absorption in photon management as explained by Wang et al [50].

As expected, since absorption coefficient and dielectric functions are directly related quantities, similar behavior is observed for dielectric functions in **Fig. 12**. Inverse behaviours of the dielectric functions along the *xx* and *zz* directions as biaxial strains are applied have been observed. Imaginary part of the dielectric function depicts the response of the compound to an outer electromagnetic field. Increased ε_{2_xx} indicates a strengthened inner electric field, which is formed by the free minority carriers; on the contrary, declined ε_{2_zz} shows a weakened electric field. Considering the DOS (**Fig. 4c**), the two major peaks observed for the imaginary part at 1.6 eV and 3.2 eV (**Fig. 12a**) can be attributed to the electron transition from Se 4p to In 5s and In 5p/Cu 4s+3d, respectively. These two peaks are blue- and red-shifted for the in-plane ε_{2_xx} component while red- and blue-shifted for the out-of-plane ε_{2_zz} one as strain goes from negative to positive values. Real parts of dielectric functions (ε_{1_xx} and ε_{1_zz}) show the same trend as that of the imaginary parts. Static dielectric constants $\varepsilon(0)$ shows larger deviation under strain for out-of-plane component than for the in-plane one.

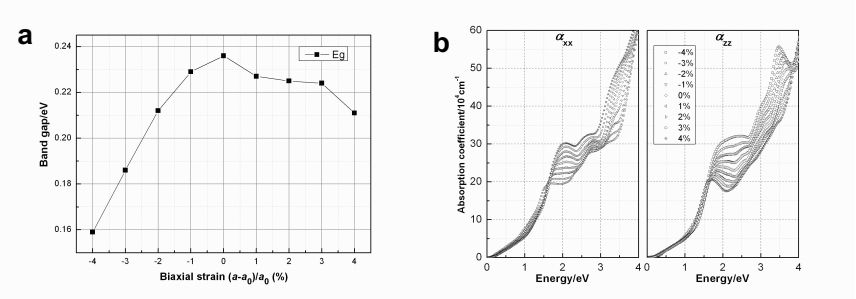

Fig. 11 Band gap vs. biaxial strain(a-a_0)/a_0(%) (a) and absorption coefficient in perpendicular (*xx*) and parallel (*zz*) directions to *c*-axis vs. incident energy for various biaxial strains (a-a_0)/a_0(%) (b).

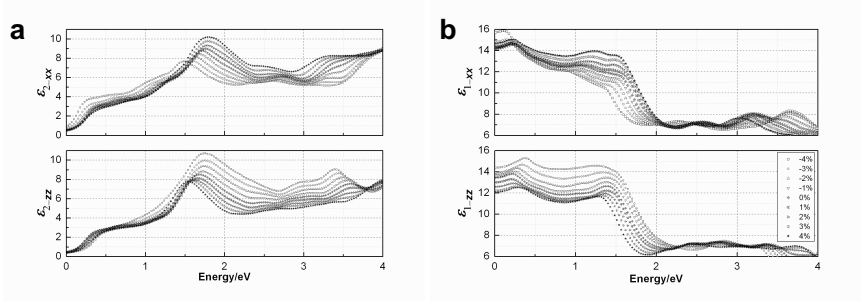

Fig. 12 Imaginary part (a) and real part (b) of dielectric functions at perpendicular (*xx*) and parallel (*zz*) directions to *c*-axis vs. incident energy for various biaxial strains (a-a_0)/a_0(%).

3.2.2 Topological properties

To better understand the evolution of electronic and optical properties as biaxial strain is applied, the topological properties at bond critic points have been studied, as presented in **Fig. 13**. Both nonsymmetrical structure I (**Fig. 13a**) and structure II (**Fig. 13d**) have been considered

separately. As it shows, strain has a weak influence on the atomic interactions. All pairwises interactions lie in the *transit* closed-shell zone, i.e. $1<|V_{BCP}|/G_{BCP}<2$, and thus correspond to covalent bond. Narrowed and broadened dispersion of covalent degrees and $|V_{BCP}|/G_{BCP}$ ratios, which can be associated to "rigid" and "loose" topological cells, respectively, are observed under compressive strains for the former and tensile strains for the latter. These two different topological cells explain the anisotropic response to electromagnetic field, such as dielectric functions. Scattered bond degree distribution reflects a large extent in bond polarity. This distribution provides information on the preferable site of maximal shared electron density and on the ease of electron transition. As we know, negative total energy density is a sign of nuclei attraction. The bare change in $|V_{BCP}|/G_{BCP}$ ratios with negligible differences among Cu-Se/Se* and In/Al-Se imply a uniform and stable bonding characteristics at compressive strain, which echoes to "rigid" cell. Similarly, the decrease in $|V_{BCP}|/G_{BCP}$ ratios with considerable differences assigns large deviation in bonding uniformity and intensity at tensile strain, which is in line with "loose" cell. One should underline that, the upward and downward changes of the bond degrees of Cu-Se/Se*and In-Se/Se* in structure II when strain is below -2% behave discordantly to those of the other strain ranges. This abnormal evolution of the bond degrees, which is also noticeable for $|V_{BCP}|/G_{BCP}$ ratios, suggests the importance in strain-controlling during PV cell manufacturing.

As bond lengths and bond angles in **Fig. 13c** and **13f** show, strain modifies the bond configuration by adjusting the displacement of bond critical point, as well as the distance from terminal atoms (M, Se) to bond critical point. In each crystal cell, there are four-centered structures of type I sandwiched along the *c*-axis by two structures of type II at each side. Structural parameters depart from the free-strained ones when unit cell is subjected to biaxial strain. Among these deviations, those pertaining to long bond lengths are higher than those pertaining to the short ones. For example, the In-Se bond length has varied more significantly than the Al-Se one, which is barely changed throughout. As we noticed previously, bond length evolves oppositely to bond angle. As to the model "n_M-b-n_{Se}", small bond angle means shorter distance from BCP to M cation than to Se anion. Displacement of BCP originates from the nuclei attraction will leads to a bond path deflection. High deflection shows large overlapping area in between shared electrons. BCP close to a M cation indicates large overlapping region in electron density with a strong electronic attraction from the M cation. Electron transition from Se anion to M cation becomes easier. By contrast, BCP close to a Se anion indicates small overlapping region in electron density, thus it is more difficult for electron to transit from Se anion to M cation. Bond angle can then be a sign of electron transition feasibility. The downward change of the band gap under both compressive and tensile strains (**Fig. 11a**) can be paralleled with the decrease of the bond angles; the faster decrease of the band gap at compressive strain is concomitant with its faster reduction of the bond angle than at tensile strain, particularly for pairwise In-Se.

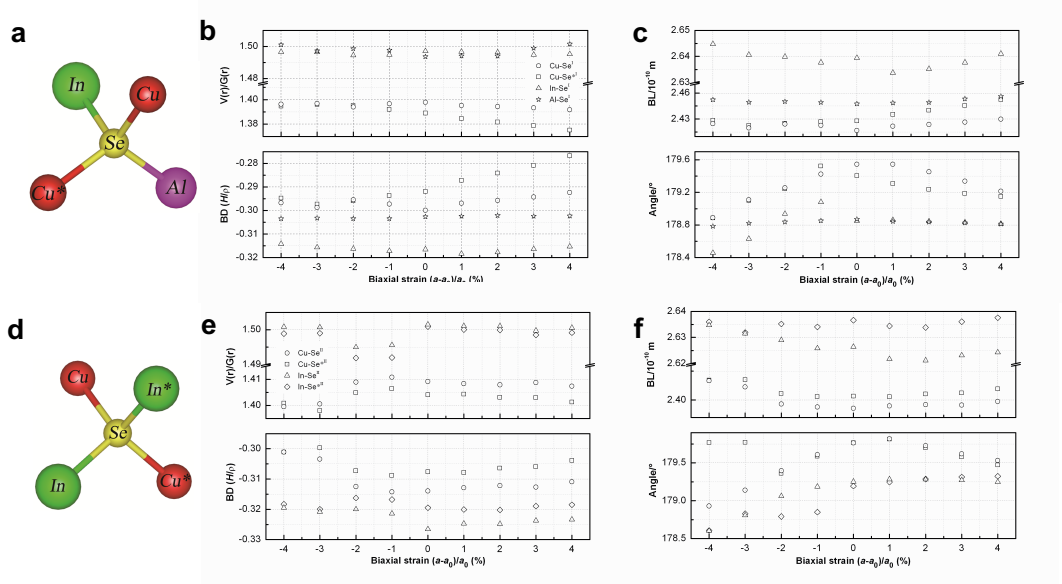

Fig. 13 Topological properties at bond critic points of structure I (a) and structure II (d) vs. biaxial strain $(a\text{-}a_0)/a_0(\%)$. (b) and (e): ratio of potential energy density to kinetic energy density $|V_{CP}|/G_{CP}$ and bond degree BD; (c) and (f): bond length BL and bond angle.

As seen above, for $CuIn_{0.75}Al_{0.25}Se_2$, i) pairwise In-Se in structure II are mainly responsible for the electron transitions when incident energy is above 1.6 eV, ii) the peaks of the in-plane dielectric function are attributed to the electron transition between Se $4p_{x/y}$-Cu $3d_{xy}$ and Se $4p_{x/y}$-Cu $3d_{x2-y2}$, while those of the out-of-plane dielectric function are assigned to the electron transition between Se $4p_z$-In 5s and Se $4p_z$-In $5p_z$, iii) under both tensile and compressive strains, covalent degrees of In-Se/Se* decrease. As we know, covalent degree stands for atomic interaction intensity and strong interaction leads to high absorption coefficient. α_{xx} goes down under compressive strain (lattice a decreases), whereas α_{zz} behaves oppositely. The decrease of α_{xx} and α_{zz} under compressive and tensile strain, respectively, can be correlated to the negative shift of the covalent bond degree of In-Se. Therefore, strengthened absorption occurs along the lengthened direction, i.e. α_{zz} at compressive strain and α_{xx} at tensile strain, which could be due to the long transportation path for incident photon providing a big chance to be absorbed before it escapes. This is consistent with the downward evolution of bond angle under strains, which gives high feasibility for electron transition.

4. Conclusions

In this study, the band structure, density of states, absorption coefficient, and dielectric functions of $CuIn_{1-x}Al_xSe_2$ have been calculated by using the full potential linear augmented plane wave (FP-LAPW) method. $CuIn_{1-x}Al_xSe_2$ has a direct band gap, its increasing value as aluminum substitutes indium contrasts with their continuously declining absorption coefficients. $CuIn_{0.75}Al_{0.25}Se_2$ has been recognized as the optimal alloy in terms of the compromise between band gap and absorption coefficient. Based on electron density ρ_{BCP}, and the $|G_{BCP}|/V_{BCP}$, H_{BCP}/ρ_{BCP} ratios at BCP, the nonequivalent M-Se bond interactions all lie in the *transit* closed-shell zone and show intermediate polar covalent interactions with positive Laplacian and negative total energy ($1<|V_{BCP}|/G_{BCP}<2$). The In-Se bond bears the largest covalent degree. As x increases, the covalent degree of pairwise Al-Se decreases. The connection established

between bond length, bond angle and bond degree for each pairwise M-Se, can be used as a tool to predict the ease of electron transition. The absorption coefficients in perpendicular and parallel direction to *c*-axis increase and decrease, respectively, as strain goes from compressive to tensile. Shrinkage and expansion of the dispersions in bond degree due to compressive and tensile strains, respectively, are responsible for the anisotropic optical responses. Inverse evolution for perpendicular and parallel components of dielectric function and absorption coefficient under strain originates from the bond asymmetry. The decrease of band gap with respect to strain is asymmetric, it decreases faster under compressive strain than tensile one. The whole set of results obtained in this work show the strong anisotropic impact of the biaxial strains on the topological and optical properties of $CuIn_{1-x}Al_xSe_2$. This suggests managing the strains as best as possible during the PV cell manufacturing, especially during epitaxial growth.

Conflicts of interest

There are no conflicts of interest to declare.

Acknowledgements

This work is financially supported by China Scholarship Council (CSC). This work was granted access to the HPC resources of the Centre Informatique National de l'Enseignement Supérieur (CINES), Montpellier, France under allocation A0050806881 made by the Grand Equipement National de Calcul Intensif (GENCI). It was also granted access to the HPC resources of Aix-Marseille Université financed by the project Equip@Meso (ANR-10-EQPX-29-01) of the program "Investissements d'Avenir" supervised by the Agence Nationale de la Recherche.

References

1 O. I. Okoro and T. C. Madueme, *Renewable Energy*, 2004, **29**, 1599–1610.

2 N. L. Panwar, S. C. Kaushik and S. Kothari, *Renewable and Sustainable Energy Reviews*, 2011, **15**, 1513–1524.

3 S. Rühle, *Solar Energy*, 2016, **130**, 139–147.

4 H. Fu, *Journal of Materials Chemistry C*, 2018, **6**, 414–445.

5 H. J. Meadows, S. Misra, B. J. Simonds, M. Kurihara, T. Schuler, V. Reis-Adonis, A. Bhatia, M. A. Scarpulla and P. J. Dale, *Journal of Materials Chemistry C*, 2017, **5**, 1336–1345.

6 O. Meglali, A. Bouraiou, N. Attaf and M. S. Aida, *Optik - International Journal for Light and Electron Optics*, 2017, **140**, 709–717.

7 M. Pandey, K. Kuhar and K. W. Jacobsen, *The Journal of Physical Chemistry C*, 2017, **121**, 17780–17786.

8 K. C. Huang, C. L. Liu, P. K. Hung and M. P. Houng, *Applied Surface Science*, 2013, **273**, 723–729.

9 W. Deng, Z. Yan, Y. Fang and Y. Wang, *Journal of Materials Science: Materials in Electronics*, 2014, **25**, 2829–2834.

10 K.-W. Cheng, K. Hinaro and M. P. Antony, *Solar Energy Materials and Solar Cells*, 2016, **151**, 120–130.

11 J. López-García and C. Guillén, *Thin Solid Films*, 2009, **517**, 2240–2243.

12 H. Salehi and E. Gordanian, *Materials Science in Semiconductor Processing*, 2016, **47**, 51–56.

13 J. M. Raulot, C. Domain and J. F. Guillemoles, *Journal of Physics and Chemistry of Solids*, 2005, **66**, 2019–2023.

14 P. Nayebi, K. Mirabbaszadeh and M. Shamshirsaz, *Physica B: Condensed Matter*, 2013, **416**, 55–63.

15 H. Salehi and E. Gordanian, *Materials Science in Semiconductor Processing*, 2016, **47**, 51–56.

16 A. Soni, V. Gupta, C. M. Arora, A. Dashora and B. L. Ahuja, *Solar Energy*, 2010, **84**, 1481–1489.

17 F. L. Tang, Z. X. Zhu, H. T. Xue, W. J. Lu, Y. D. Feng, Z. M. Wang and Y. Wang, *Physica B: Condensed Matter*, 2012, **407**, 4814–4818.

18 R. F. W. Bader, *Atoms in molecules: a quantum theory*, Clarendon Press, Oxford, 1990.

19 G. Gervasio, R. Bianchi and D. Marabello, *Chemical Physics Letters*, 2004, **387**, 481–484.

20 P. Mori-Sánchez, A. M. Pendás and V. Luaña, *Journal of the American Chemical Society*, 2002, **124**, 14721–14723.

21 E. Espinosa, I. Alkorta, J. Elguero and E. Molins, *The Journal of Chemical Physics*, 2002, **117**, 5529–5542.

22 S. Ullah, H. U. Din, G. Murtaza, T. Ouahrani, R. Khenata, Naeemullah and S. Bin Omran, *Journal of Alloys and Compounds*, 2014, **617**, 575–583.

23 J. Jalilian, M. Naseri, S. Safari and M. Zarei, *Physica E: Low-dimensional Systems and Nanostructures*, 2016, **83**, 372–377.

24 C. K. Ghosh, D. Sarkar, M. K. Mitra and K. K. Chattopadhyay, *Journal of Physics D: Applied Physics*, 2013, **46**, 395304.

25 C. K. Ghosh, D. Sarkar, M. K. Mitra and K. K. Chattopadhyay, *Journal of Physics: Condensed Matter*, 2012, **24**, 235501.

26 P. Pluengphon and T. Bovornratanaraks, *Solid State Communications*, 2015, **218**, 1–5.

27 P. Blaha, K. Schwarz, G. K. H. Madsen, D. Kvasnicka and J. Luitz, *WIEN2k, an augmented plane wave+local orbitals program for calculating crystal properties Karlheinz Schwarz, Techn. Universität Wien, Austria*, 2001.

28 D. C. Langreth and J. P. Perdew, *Physical Review B*, 1980, **21**, 5469–5493.

29 H. J. Monkhorst and J. D. Pack, *Physical Review B*, 1976, **13**, 5188–5192.

30 I. V. Bodnar, I. N. Tsyrelchuk and I. A. Victorov, *Journal of Materials Science Letters*, 1994, **13**, 762–764.

31 A. Otero-de-la-Roza, E. R. Johnson and V. Luaña, *Computer Physics Communications*, 2014, **185**, 1007–1018.

32 J. Parkes, R. D. Tomlinson and M. J. Hampshire, *Journal of Applied Crystallography*, 1973, **6**, 414–416.

33 O. Madelung, *Semiconductors: data handbook.*, Springer, Berlin, Heidelberg, Marburg, Germany, third., 2004.

34 N. Kodan, S. Auluck and B. R. Mehta, *Journal of Alloys and Compounds*, 2016, **675**, 236–243.

35 F. Tran and P. Blaha, *Physical Review B*, , DOI:10.1103/PhysRevB.83.235118.

36 L. Pauling, *The nature of the chemical bond and the structure of molecules and crystals: an introduction to modern structural chemistry*, Ithaca Cornell University Press, New York, third., 1960.

37 J. A. Duffy, *Physics and Chemistry of Glasses*, 2001, **42**, 151–157.

38 A. S. Verma, *physica status solidi (b)*, 2009, **246**, 192–199.

39 M. I. Alonso, J. Pascual, M. Garriga, Y. Kikuno, N. Yamamoto and K. Wakita, *Journal of Applied Physics*, 2000, **88**, 1923–1928.

40 M. I. Alonso, K. Wakita, J. Pascual, M. Garriga and N. Yamamoto, *Physical Review B Condensed Matter*, 2001, **63**, 1–11.

41 G. B. Rybicki and A. P. Lightman, in *Radiative process in astrophysics*, Wiley-Interscience, 1985, p. 14.

42 D. R. Penn, *Physical Review*, 1962, **128**, 2093–2097.

43 L. Yu and A. Zunger, *Physical Review Letters*, 2012, **108**, 068701.

44 W. Yin, T. Shi and Y. Yan, *Advanced Materials*, 2014, **26**, 4653–4658.

45 J. Hernández-Paredes, R. C. Carrillo-Torres, A. A. López-Zavala, R. R. Sotelo-Mundo, O. Hernández-Negrete, J. Z. Ramírez and M. E. Alvarez-Ramos, *Journal of Molecular Structure*, 2016, **1119**, 505–516.

46 C. Katan, P. Rabiller, C. Lecomte, M. Guezo, V. Oison and M. Souhassou, *Journal of Applied Crystallography*, 2003, **36**, 65–73.

47 P. Popelier, *Coordination Chemistry Reviews*, 2000, **197**, 169–189.

48 R. F. W. Bader and H. Essén, *The Journal of Chemical Physics*, 1984, **80**, 1943–1960.

49 T. Wada, S. Nakamura and T. Maeda, *Progress in Photovoltaics: Research and Applications*, 2012, **20**, 520–525.

50 H. P. Wang, D. H. Lien, M. L. Tsai, C. A. Lin, H. C. Chang, K. Y. Lai and J. H. He, *Journal of Materials Chemistry C*, 2014, **2**, 3144–3171.